Robustness of attosecond molecular modes under nuclear dynamics

Wan-Dong Yu [1,*] Lei Geng [1] and Liang-You Peng [1,2,3,4,†]

[1] *State Key Laboratory for Mesoscopic Physics and Frontiers Science Center for Nanooptoelectronics, School of Physics, Peking University, Beijing 100871, China*

[2] *Collaborative Innovation Center of Quantum Matter, Beijing 100871, China*

[3] *Collaborative Innovation Center of Extreme Optics, Shanxi University, Taiyuan 030006, China*

[4] *Peking University Yangtze Delta Institute of Optoelectronics, Jiangsu, Nantong 226010, China*

(Received 17 May 2023; revised 22 October 2023; accepted 21 November 2023; published 8 December 2023)

We investigate the impact of nuclear motion on attosecond charge migration modes, characterized by low-frequency and long-distance hole density patterns in polyatomic molecules. We create the initial hole density using constrained density functional theory and track the subsequent electron-ion dynamics using the Ehrenfest dynamics together with the time-dependent density functional theory. Our focus is on a prototypical BrC_4H system, where we examine the effects of alterations in initial nuclear geometry. We find that the nuclear motion drives and transforms the charge migration modes, underscoring the strong connection between hole patterns and nuclear dynamics. For various initial stretches or bends, these modes demonstrate considerable robustness to the nuclear motion, i.e., they do not dissipate under the classical nuclear motion throughout the computational time. We discover that the charge migration modes correspond to prominent peaks in the frequency spectra of the electronic dipole moment. Additionally, our calculations indicate that the modes primarily originate from the last four atoms near the halogen site and are predominantly attributed to the hole density closest to these nuclear trajectories. Our study offers insights into the behavior of the charge migration modes under varying nuclear geometry and may have implications for understanding related nuclear effects.

DOI: 10.1103/PhysRevA.108.062807

I. INTRODUCTION

When a molecule absorbs energy from the stimulus, such as laser pulses or chemical reactions, electrons can be excited from their ground state to higher-energy levels. This can cause the charge (i.e., electrons or holes) migrates from one region of the molecule to another, leading to the redistribution of charge. The study of charge migration (CM) is of fundamental importance to the field of attosecond science [1–3], where it is possible to experimentally track and control the ultrafast motion of charges within molecules on timescales of femtoseconds (fs) to attoseconds [4–7]. Since the CM happens usually as the first step following the photoionization or photoexcitation, the control of CM dynamics can drive the subsequent nuclear motion to a favorable reactive path or fragmentation product [8], which is also important for understanding and designing chemical reactions and molecular devices.

Since the complexity of CM arises from the interplay of many factors, such as the electronic structure of the molecule and electronic correlations, the full range of CM mechanisms in molecules remains elusive. In the absence of the nuclear motion, theoretical studies showed that CM can be solely driven by electronic correlations [9–12] and identified a variety of mechanisms that can give rise to CM. These mechanisms include the attosecond response of the electrons to fill the exchange-correlation hole [13], the initial-state dependence [14], the bond hopping mechanism [15], and the two-state coherence oscillation [16], among others.

However, the coupling between the electronic and nuclear degrees of freedom introduces additional complexities and challenges, which must be addressed to fully understand the CM mechanism. Such electron-nuclear coupling can be discussed with various theoretical methods at different levels. One common approach is the Ehrenfest approximation [17,18], where nuclei are treated as classical particles moving on electronic mean-field potentials. The Ehrenfest method has provided insights into how the nuclear motion affects the CM in different cases, for example, by sustaining or disrupting certain charge oscillations [19–23]. By taking into account the quantum nature of nuclear motion, researchers have studied the decoherence and recoherence in polyatomic molecules [24–28]. These methods, with both quantum and classical treatments of the nuclear motion, investigate from a variety of perspectives and reveal the complexity of nuclear motion on CM.

In this work, we study the effects of nuclear motion on attoscond molecular modes. These molecular modes refer to hole density oscillations across the entire molecular skeleton, characterized by low characteristic frequencies ($\sim$1 eV) and long-distance migration (up to $\sim$17 Å) between the two ends of a molecule [29,30]. Using the frozen nuclei approximation, the attosecond modes exhibit certain intriguing features. For instance, Folorunso *et al.* showed that the speed of hole

*wandongyu@pku.edu.cn

†liangyou.peng@pku.edu.cn

migration saturates as the length of the carbon chain increases [29]. Mauger *et al.* recently found that the modes are sensitive to initial conditions and suggested a possible soliton-mode mechanism [31]. Although these hole modes have been identified in polyatomic molecules, such as halogenated hydrocarbon chains [29,32] and halogenated aromatic rings [33], the underlying mechanism of the molecular modes and their coupling with the nuclear motion remain not fully understood.

Based on the Ehrenfest dynamics together with the time-dependent density functional theory (Ehrenfest-TDDFT), we focus our study on the effects of nuclear motion on the attosecond molecular modes. We find that the attosecond modes exhibit a certain degree of robustness against the nuclear motion. By initially stretching or bending the molecular geometry, we investigate the effects of molecular structure and find that the modes persist despite the classical nuclear motion. Nuclear motion alters the frequencies of the modes through sideband effects or frequency modulation. Furthermore, the CM modes contribute distinct continuous low-frequency signatures to the frequency spectrum of the electron dipole moment. Our calculations are conducted on a prototypical molecule, i.e., BrC_4H. This molecule can be oriented using the impulsive orientation technique [5,34] and the presence of the attosecond modes is a common feature among halogenated hydrocarbon chains [29].

Compared with previous studies of CM modes with the frozen nuclei approximation, a fundamental difference in this work is that we adopt the same initial conditions, but allowing the nuclei to move as classical points of charge at the onset of the dynamics. To trigger the CM modes, it is usually necessary to create coherent states that constrain a unit hole on the functional site of the molecular cation. This mimics the localized nonstationary hole state after the strong-field ionization [5], where the molecular functional group typically exhibits high sensitivity to the interacting laser pulse [8]. Such a coherent hole state is associated with multiple electronic orbitals, contrasting with the *ad hoc* ionization resulting from the sudden removal of a single electron from an orbital [35].

It is worth noting that Ehrenfest dynamics has limitations in simulating the long-lasting charge migration [36]. On one side, the Ehrenfest method lacks the electronic decoherence, which may lead to incorrect asymptotic behaviors with the moving nuclei. Additionally, the single trajectory Ehrenfest method we used does not account for any nuclear quantum effects due to the assumption of nuclei as classical points of charge, potentially leading to the decoherence on the timescale of several femtoseconds [22]. This decoherence can be partially addressed by using multiple trajectories [37]. On the other side, in polyatomic molecules, fully quantum calculations have demonstrated that the coupling between electronic and nuclear dynamics usually causes rapid decoherence on the timescale of several femtoseconds [27,38,39]. Therefore, in this work, the long-time simulations limit the discussion to the effects of classical nuclear motion. Our goal is to set up specific initial conditions to better understand how the electronic dynamics interacts with the nuclear motion and how this might affect the attosecond modes.

The rest of the paper is organized as follows. In Sec. II, we first introduce the constrained density functional theory (CDFT) method for the hole initialization. The CDFT method is only used to create the initial electronic coherence, which imitates the site-specific hole state after the strong-field ionization. Then, we introduce the Ehrenfest-TDDFT. Numerical details are given in Sec. II C, including all the key parameters and concrete steps to initialize the electron-ion dynamics. In Sec. III, we study the CM modes and the nuclear effects. The results are summarized in Sec. IV. Throughout this paper a.u. refers to atomic units.

II. METHODS

A. Initial conditions for CM modes

We consider CM modes in the molecular ion with an electron ionized from the highest occupied molecular orbital (HOMO). To trigger the CM modes, one usually needs to create a coherence initial hole state that constrains a unit hole on a specific site of the molecular cation. This is achieved by using the constrained density functional theory (CDFT) [40,41], which was shown to be a valuable method for electronic structure calculations. More details of the CDFT can be found in the review articles [42,43] and references therein.

A standard CDFT framework allows for the incorporation of multiple constraints in a many-electron system. In this work, we only consider the density constraint, which imposes the electronic density on specific site of a molecule. Suppose there are, in total, m density constraints acting on an N-electron system, which satisfy the following constraint equations:

$$\int w_k^\sigma(\mathbf{r})\rho_\sigma(\mathbf{r})d\mathbf{r} - F_k^\sigma = 0, \tag{1}$$

where ρ_σ is the electronic density for the σ-spin channel. The F_k^σ is the value of the kth constraint, describing the charge imbalance between the constrained site and the rest. ω_k^σ is the weight function of the kth constraint, which has several options, such as the Mulliken population [44], the Löwdin population [45], the real-space Becke [46], the Hirshfeld partition [47], and so on. In this work, we employ the Hirshfeld partition method to generate the weight function.

To obtain the initial electronic state, one usually self-consistently solves the following equations with constraint potentials:

$$\left[H_{\mathrm{KS}} + \sum_{k=1}^{m} \lambda_k w_k^\sigma(\mathbf{r})\right]\phi_{i,\sigma}(\mathbf{r}) = \varepsilon_i\phi_{i,\sigma}(\mathbf{r}), \tag{2}$$

where $\phi_{i,\sigma}$ is the ith σ-spin Kohn-Sham orbital and λ_k is the kth constraint factor. H_{KS} is the standard Kohn-Sham (KS) Hamiltonian

$$H_{\mathrm{KS}} = -\frac{\nabla^2}{2} + V_{\mathrm{H}} + V_{\mathrm{xc}} + V_{\mathrm{en}}, \tag{3}$$

where V_{H} is the Hartree potential, V_{xc} is the exchange-correlation potential, and the V_{en} is the electron-nuclei potential. Thus, Eq. (2) represents the standard KS equation, with the exception of the additional weight potentials ω_k^σ. By solving Eqs. (1) and (2) together in a self-consistent manner to obtain the values of λ_k and $\phi_{i,\sigma}$, the constraints are effectively satisfied. For more information about the computational

optimization of the CDFT method, please see Refs. [48,49] and the references therein.

It should be noted that the CDFT is solely used to generate the site-specific hole density following the strong-field ionization and is not employed during the time-dependent propagation. Therefore, the initial CDFT hole state ceases to be a stationary state of the time-dependent Hamiltonian ($H_{\rm KS}$), and the system begins to evolve in time.

B. Ehrenfest-TDDFT method

To investigate the interdependent electron and nuclear dynamics, we utilize the Ehrenfest-TDDFT method [18]. This approach considers electronic correlations, the nuclear motion, and nonadiabatic effects, and it has proven effective in understanding the electron-ion dynamics [50–52]. In the Ehrenfest-TDDFT, the electron dynamics is described quantum-mechanically by the time-dependent Kohn-Sham (TDKS) equations [53], nonadiabatically coupling to the ionic dynamics described by the Ehrenfest method [17]

$$i\frac{\partial\phi_{j,\sigma}(\mathbf{r},t)}{\partial t} = \Big[-\frac{1}{2}\nabla^2 + V_{\rm H}[\rho](\mathbf{r},t) + V_{\rm xc}[\rho](\mathbf{r},t) + V_{\rm en}(\mathbf{r},\{\mathbf{R}(t)\})\Big]\psi_{j,\sigma}(\mathbf{r},t), \tag{4}$$

$$M_I\frac{d^2\mathbf{R}_I(t)}{dt^2} = -\nabla_{\mathbf{R}_I}\Big[\int d^3\mathbf{r}\rho(\mathbf{r},t)V_{\rm en}(\mathbf{r},\{\mathbf{R}(t)\}) + \frac{1}{2}\sum_{I\neq J}^{N_{\rm ion}}\frac{Z_I Z_J}{|\mathbf{R}_I(t)-\mathbf{R}_J(t)|}\Big], \tag{5}$$

where $\psi_{j,\sigma}(\mathbf{r},t)$ are the TDKS orbitals, and the nuclear motion couples to the total electronic density $\rho(\mathbf{r},t)$. $\mathbf{R}_I(t)$ are the nuclear coordinates and $N_{\rm ion}$ is the total number of nuclei. M_I and Z_I are, respectively, the mass and charge of the Ith nuclear.

C. Numerical details

All the calculations are carried out using the OCTOPUS program [54]. The CDFT of the electronic density constraint is implemented in a developer version [32]. All numerical quantities are discretized in a cubic box ($48\times48\times60$ a_0^3) with a uniform grid spacing of 0.27 a_0, where a_0 is the Bohr radius. The atomic core electrons are handled with norm-conserving pseudopotentials [55]. We employ an adiabatic local density approximation [56] for the electronic exchange-correlation functional.

To prepare the initial conditions for the nuclear geometries and the CDFT electronic state, we follow a three-step process. (i) We optimize the molecular structure of the neutral BrC_4H and obtain its nuclear equilibrium positions. (ii) We consider two different approaches to initialize the nuclear geometry. In the first method, we stretch the bond length of the terminal carbon-bromine (C–Br) bond with various percentages, while in the second method, we bend the C–Br bond with different angles. (iii) We perform CDFT calculations to constrain a unit hole on the Br atom. We begin by setting the population of an electron in the HOMO to zero. Then, maintaining the same electronic configurations, we perform the CDFT calculations for the $[BrC_4H]^+$ cation [32].

In this work, initializing the hole using CDFT is crucial. This is because the hole state, when initialized by the CDFT, typically results in a stronger charge current and more pronounced oscillating modes compared to directly ionizing an electron from the HOMO of the density functional theory (DFT) ground state [35].

At the beginning of the time-dependent propagation, the constraint potential is removed. This causes the initial CDFT state to be nonstationary (i.e., a coherent superposition of cationic eigenstates) and the forces acting on the nuclei are not balanced. Consequently, the system undergoes dynamic evolution, which is tracked by the Ehrenfest-TDDFT method. During the time-dependent calculations, a velocity Verlet algorithm is used to propagate the nuclear coordinates [57]. The time step for each iteration is fixed to 8.46×10^{-4} fs. The total propagation time is up to 120 fs, unless the ion dynamics stably evolves over several vibrational periods.

In this paper, we present a modified definition of the time-dependent hole density that is crucial for visualizing CM modes in molecules when the nuclei are allowed to move. This definition is introduced prior to our results, as it is necessary for understanding the subsequent analyses that demonstrate its correlation with the nuclear motion and the frequency spectra of electronic dipole moment. Specifically, the time-dependent three-dimensional hole density is defined as the difference between the instantaneous DFT electronic density of the neutral molecule and the time-dependent electronic density of the cation obtained from the TDDFT,

$$\rho^{\rm H}[\mathbf{r},\mathbf{R}(t),t] = \rho^0_{\rm DFT}[\mathbf{r},\mathbf{R}(t),t] - \rho^+[\mathbf{r},\mathbf{R}(t),t], \tag{6}$$

where $\mathbf{R}(t)$ represents nuclear coordinates for a specific nuclear geometry, ρ^+ is the cationic electronic density obtained from the TDDFT, and $\rho^0_{\rm DFT}$ is the instantaneous DFT electronic density with the nuclear geometry at the same time t. Importantly, with the frozen nuclei approximation, this definition reverts to the conventional one used in previous studies, and there is no contradiction with those cases. In Sec. III, we discuss the modified definition and provide a comparison by illustrating the hole density obtained using the neutral electronic density at $t=0$.

III. RESULTS AND DISCUSSION

In this section, we examine the CM modes of BrC_4H following the ionization and explore how the nuclei affect the process, including changes to the initial nuclear geometry and the nuclear motion.

We begin our simulations by placing the linear $[BrC_4H]^+$ cation on the Z axis and stretching the terminal C_d–Br bond length by various percentages relative to the neutral ground-state nuclear geometry. Specifically, we stretch the Br atom, while keeping the other atoms initially fixed at their positions in the neutral ground-state molecule. For reference, the 0% case corresponds to initializing all nuclear positions at the neutral ground-state geometry. Due to the axial symmetry of the linear molecule under the stretch, we analyze the time-dependent one-dimensional integrated hole density on the Z

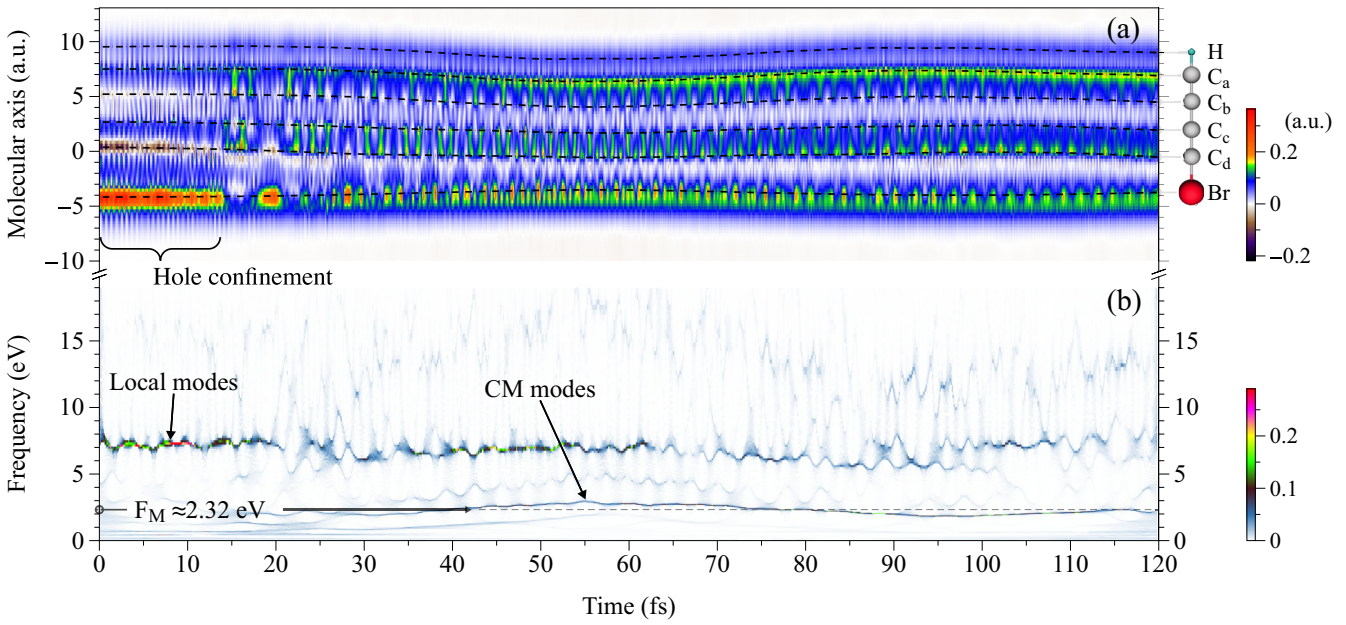

FIG. 1. Dynamical properties for the initial 36.01% stretch of the C_d–Br bond length. The other bond lengths are initially the same as the neutral ground-state molecule. The molecular ion is linear and aligned on the Z axis. (a) Time evolution of the one-dimensional integrated hole density $\rho^h(z,t)$. Dashed lines: Nuclear positions on the molecular axis, from the top to the bottom corresponding to H, C_a, C_b, C_c, C_d, and Br. The schematic diagram of the molecular shape is drawn to guide the eyes. Color bar labels the hole density in atomic units. (b) Time-frequency analysis of the electronic dipole moment. F_M: The frequency of CM modes with the maximum intensity. Color bar labels the intensity of frequency spectrum.

axis for convenience, which is defined as

$$\rho^h(z,t) = \iint \rho^H[x,y,z,\mathbf{R}(t),t]dxdy. \tag{7}$$

In this study, we provide a detailed examination of the impact of the nuclear motion on CM modes. To illustrate this, we utilize a representative example where the terminal C–Br bond length is initially stretched by 36.01%. This scenario is chosen specifically because it embodies universal outcomes that shed light on the behavior of CM modes. By investigating this typical case, we aim to unravel the key characteristics of CM modes under the nuclear motion. Figure 1(a) depicts the time evolution of the hole density, $\rho^h(z,t)$, with this specific initial condition. At $t = 0$, the hole density is confined to the Br atom, and during the first ∼15 fs, most of the holes remain localized around the Br site. At this stage, we observe no significant CM modes, indicating that there is no notable migration of the holes across the molecular skeleton between the Br and the terminal C_a–C_b bond. However, as the simulation progresses, pronounced CM modes emerge between 15 and 120 fs, driven by the nuclear motion. The initial stretch of the C_d–Br bond length traps the hole on the Br atom, and then, due to intramolecular energy transfer, the nuclear motion releases the hole and causes it to migrate across the whole molecular skeleton. For the neck structure observed at approximately 55 fs, it is noticeable that not all nuclear distances reach their minimum values concurrently. Only the bond lengths involved in the attosecond modes (i.e., bonds between C_b and Br), maintain their minimum values during this phase. These results suggest that CM modes are intimately connected with the nuclear motion and provide valuable insights into the mechanisms governing the hole migration in the $[BrC_4H]^+$.

It is worth noting that the hole patterns in Fig. 1(a) are computed using the modified hole definition presented in Eq. (7), rather than the neutral DFT density at $t = 0$ (see Appendix A for a detailed comparison). This comparison demonstrates that Eq. (7) reveals some latent properties of CM modes under the nuclear motion. Specifically, when the nuclei begin to move, Eqs. (6) and (7) ensure that, at each time step, the DFT orbitals used to construct the neutral density are *natural orbitals* [16]. These orbitals diagonalize the density operator and are eigenstates of the time-dependent Hamiltonian, which helps alleviate the spatial mismatch between the neutral and cationic density that arises from the nuclear motion. As a result, our modified hole definition provides an advantage over the hole definitions using the fixed neutral density.

One can observe from Fig. 1(a) that the hole confinement in specific regions of the molecule may be related to high-frequency local oscillations, while CM modes tend to appear at lower frequencies. This observation encourages us to further investigate the frequency spectra of hole modes and explore possible connections with the electronic dynamics. Our analysis reveals that CM modes correspond to prominent continuous low-frequency signatures in the electronic dipole moment's frequency spectra. On the other hand, the hole confinement in certain molecular regions is mainly associated with high-frequency electronic dipole oscillations.

To illustrate this, we present the time-frequency analysis of the electronic dipole moment in Fig. 1(b). We employ the wavelet-induced mode extraction (WIME) method [58,59], which is particularly well suited for extracting oscillating components that form amplitude modulated-frequency modulated (AM-FM) signals. This analysis offers insights into the changes of intramolecular oscillating modes. During the

initial 20 fs, most frequency components are found in the high-frequency range of 7–8 eV. This is consistent with the observation in Fig. 1(a) that local modes are trapped in specific parts of the molecule during this stage. Following this period, the local modes persist, and concurrently, distinct continuous low-frequency signatures emerge, shifting into the 2–3 eV range. These signatures are identified as the CM modes, which are notably modulated by the nuclear motion. For instance, at around 55 fs, the nuclear relative distances are nearly at their smallest, creating a neck structure in the hole density patterns observed in Fig. 1(a). Consequently, the CM modes exhibit their highest frequency. In contrast, at around 95 fs, when the nuclear relative distances increase, the CM frequencies decrease. This observation also suggests that as nuclei approach each other, the hole density takes less time to traverse the molecular skeleton.

Although the nuclear motion in Fig. 1 does not destroy the modes after the long-time propagation, it does not imply that the charge migration lasts indefinitely. Advanced quantum simulations have shown that the nuclear motion typically causes decoherence within a few femtoseconds [39]. In polyatomic molecules, decoherence usually makes the evolving electronic wave function act as a statistical ensemble of electronic states, rather than a coherent superposition of them. However, the Ehrenfest method considers the total wavefunction as a single product of its electronic and nuclear components. So, the electronic wavefunction cannot decohere in this method, as all populated electronic states involve with the same nuclear geometry. This omission of electronic decoherence might impact the persistence of the oscillatory charge migration observed in Fig. 1.

To investigate the intramolecular spatial distributions of the CM frequency and its correlation with the electronic dynamics, we perform a windowed Fourier transform on the electronic dipole moment and conduct a space-frequency analysis of the hole density. Figure 2(a) presents the results of the space-frequency analysis of the hole density. In the frequency region of 2–3 eV, we observe a distinct pattern of four separate spots with nearly identical peak frequencies located in the spatial regions of three C–C bonds and one C–Br bond. This suggests that these four spots correspond to the same oscillating mode distributed along the molecular skeleton, i.e., the CM modes. The maximum intensity is located at a frequency of $F_M \approx 2.32$ eV. Alongside the F_M frequency, sidebands are present, which are attributed to nuclear effects. For comparison, we examine the CM dynamics with the frozen nuclei approximation. As demonstrated in Appendix B, the frozen-nuclei CM frequencies appear cleaner and the electronic dipole spectrum does not exhibit spiny splits. In Fig. 2(b), we identify that the F_M corresponds to a pronounced peak in the frequency spectra of the electronic dipole moment. This observation establishes a connection between the CM modes and the frequency spectra of electronic density evolution, which implies that the modes might be controlled by ultrafast laser pulses.

While the time evolution of hole density and frequency analysis provide some insights into nuclear effects, further clarification is needed to understand the correlation between CM modes and the nuclear motion. In this study, we find that CM frequencies are largely influenced by nuclear positions.

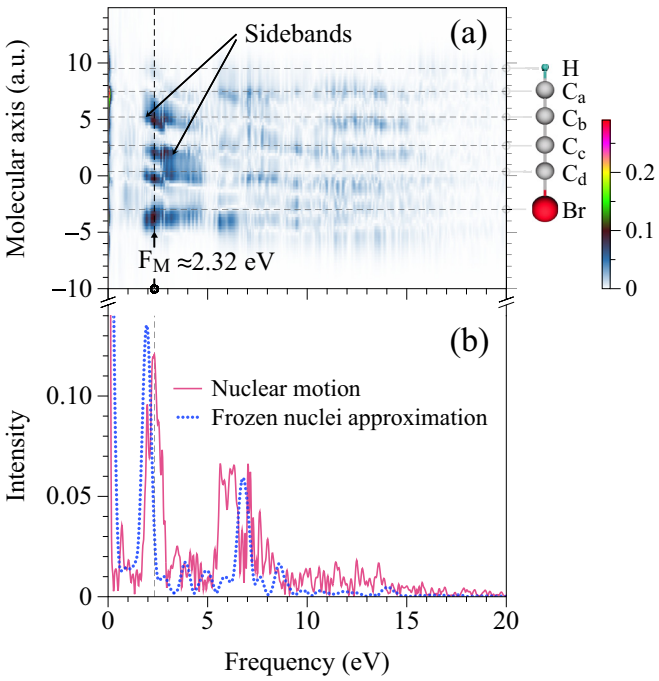

FIG. 2. Frequency analysis of the charge dynamics for the initial 36.01% stretch of the C_d–Br bond length. (a) Space-frequency analysis for the hole density. F_M: The frequency of CM modes with the maximum intensity. Dashed horizontal lines: Nuclear positions of the neutral ground-state BrC_4H as reference. Color bar labels the hole density in atomic units. (b) Frequency spectrum of the electronic dipole moment. Solid curve: Results with moving nuclei for the initial 36.01% stretch of the C_d–Br bond length. Dotted curve: Results with frozen nuclei approximation copied from Appendix B for comparison.

To better illustrate this relationship, we compute the hole frequencies along the nuclear path, defined as the Fourier transform of the integrated hole density closest to the nuclear trajectory

$$F_i^P(\omega) = \mathbb{FT}\left(\int_{S_i} \rho^H[\mathbf{r}, \mathbf{R}(t), t] dv \right), \tag{8}$$

where S_i is the trajectory for nucleus i and dv is the volume of integration closest to S_i. In this work, the size of dv is fixed as the grid volume, 0.27^3 a_0.

Figure 3 displays the hole frequencies along nuclear trajectories. We observe a nuclear effect, with distinct peaks around F_M appearing on the final four nuclear trajectories of C_b, C_c, C_d, and Br, as opposed to those of H and C_a. These four peaks exhibit comparable intensities and contribute to the CM modes. Our findings suggest that nuclear positions and their potentials are crucial factors in determining the intramolecular hole migration. This is consistent with previous research using the frozen nuclei approximation, which showed that the hole density typically emerges close to nuclei [29]. Furthermore, we observed a significant correlation between the pronounced bimodal and unimodal peaks, situated around 2.7 and 2.9 eV, and bond vibrations. The width of the bimodal split (1.4 eV) approximately equates to half of the vibrational frequency of each carbon bond (e.g., C_aC_b, C_bC_c, C_cC_d), and the unimodal splits compared to F_M (≈3.8 eV) are closely aligned with the

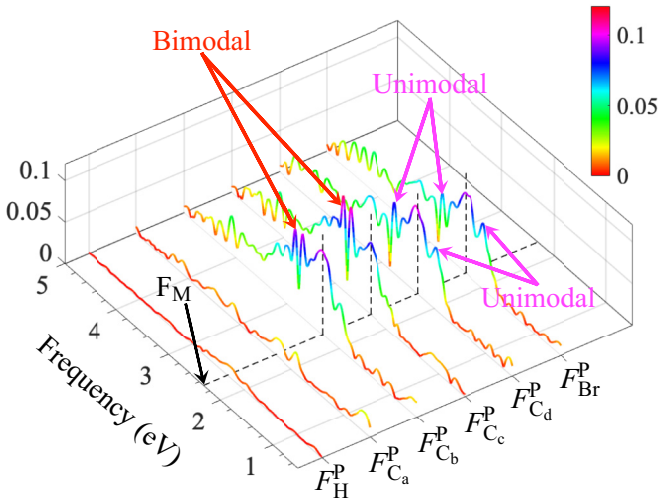

FIG. 3. Waterfall plot for the frequency spectrum of the hole density along nuclear trajectories. Dashed black lines at $F_M = 2.32$ eV are drawn to guide the eyes. Color bar labels the intensity of frequency spectrum.

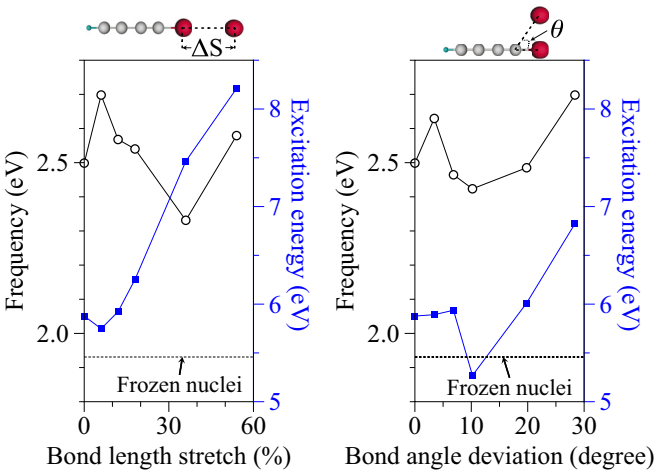

FIG. 4. CM frequencies and excitation energy with different initial stretches (left) or bends (right) of the C_d–Br bond length. Open circles: F_M. Solid squares: excitation energy. Dashed horizontal lines: F_M with the frozen nuclei approximation.

vibrational frequency of the HC_a bond. We therefore speculate that the peaks observed between 2.7 and 2.9 eV might originate from frequency dispersions caused by coupling to nuclear vibrations. In our current study, when the nuclear motion is permitted, we find that the positions of the four nuclei serve as anchors. As nuclear positions change, hole density distributions and CM modes adapt accordingly, emphasizing the significance of nuclear potentials in shaping intramolecular hole dynamics.

The results presented above demonstrate the CM dynamics for an initial stretch of the C_d–Br bond length by 36.0%, corresponding to an initial 1.2 a_0 stretch of the C_d–Br bond. To establish the generality of our findings, we perform calculations for two additional initial nuclear geometries. First, we consider the initial 1.2 a_0 stretch of the terminal C_a–C_b bond. As depicted in Fig. 7 in Appendix C, the nuclear motion introduces more spiky frequency splits into the electronic dipole spectrum. The space-frequency analysis reveals that the maximum intensity of the CM modes is 2.35 eV, which clearly corresponds to the peak in the electronic dipole spectrum. Hole frequencies along the nuclear path (not shown) further confirm that the hole density is concentrated around nuclear trajectories of the C_b, C_c, C_d, and Br. Second, we examine the initial bend of the C_d–Br bond length towards the Y direction, with a 10.21-degree bond angle deviation. For ease of analysis, we decompose the hole frequencies into two orthogonal axes, Y and Z, as displayed in Figs. 8(a) and 8(b) in Appendix D, respectively. The modes in the Y direction exhibit a peak at the same F_M of 2.42 eV as the modes in the Z direction, suggesting that they are oscillation components of the same CM modes.

For all other cases involving initial bends and stretches examined in this study, we do not observe any fundamental differences. Our results consistently indicate that the CM modes correspond to distinct peaks in electronic dipole spectra and are associated with nearly coincident peaks in the frequencies of hole density along the final four nuclear trajectories (i.e., C_b, C_c, C_d, and Br).

In Fig. 4, we extract the frequency of CM modes with the maximum intensity (i.e., F_M) and the excitation energy for various bond length stretches and bond angle deviations. The excitation energy is defined as the total energy difference compared to the ground-state total energy of the cation. We utilize dashed horizontal lines to represent a specific F_M value of 1.93 eV. This value is obtained from Appendix B, where computations were carried out using neutral nuclear equilibrium positions with the frozen nuclei approximation. Overall, taking into account the nuclear effects, the F_M values are generally 0.5 eV higher than those calculated using the frozen nuclei approximation. The excitation energy experiences a variation of approximately 2 eV for both stretch and bend cases. More significantly, we observe that the F_M values fluctuate around a median value of 2.5 eV without exhibiting any single increasing or decreasing trend. This observation offers another perspective on the impact of the nuclear motion on CM modes, revealing that CM frequencies demonstrate a certain degree of robustness to the nuclear motion.

IV. CONCLUSION

Based on the Ehrenfest-TDDFT method, we investigated the influence of the nuclear motion on CM modes. In this study, the CM modes refer to attosecond modes of hole density in polyatomic molecules, characterized by low frequencies and long-distance migration across the whole molecular skeleton. We examined nuclear effects in a prototypical linear BrC_4H system, considering changes to the initial nuclear geometry and the nuclear motion. By employing a modified hole density, we find that the nuclear motion can drive and convert CM modes, indicating a close relationship between CM modes, hole patterns, and the nuclear dynamics. With the frozen nuclei approximation, the modified hole density reverts to the conventional hole definition, yielding results consistent with previous findings. Our frequency analysis

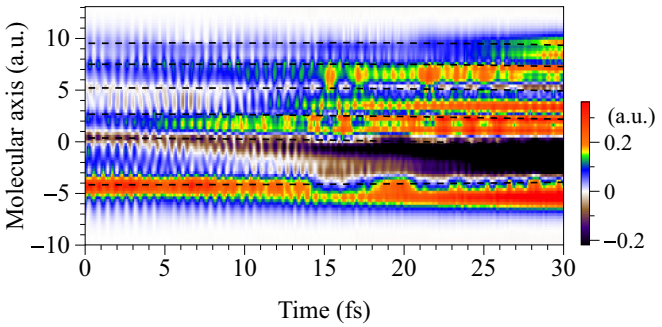

FIG. 5. Time evolution of the one-dimensional integrated hole density for the initial 36.01% stretch of the C_d–Br bond length. The hole density is calculated by Eq. (A1). Color bar labels the hole density in atomic units.

reveals that the frequency of CM modes with the maximum intensity (F_M) corresponds to a distinct peak in the electronic dipole moment's frequency spectra. This suggests that hole mode measurements could be achieved by alternatively detecting electronic dipole oscillations. Through calculations of hole density frequency spectra along nuclear trajectories (F_i^P), we determined that CM modes primarily originate from the last four atoms near the halogen site. To demonstrate generality, we computed various bond stretches and bends, finding no fundamental differences in the results. Interestingly, despite the CM modes' ability to couple with the nuclear motion, we observed a considerable robustness of the F_M to the nuclear motion.

Our findings may hold implications for future research. Theoretically, the CM modes cannot be washed out by the classical nuclear motion. This feature is also characterized by the variation of F_M around a median value of 2.5 eV under different initial stretches and bends. Experimentally, the detection of hole migration modes could be achieved by alternatively resolving the frequency spectra of the electronic dipole moment. Given that the electronic dipole can interact with external potentials, CM modes may be controllable via laser pulses or detectable using the attosecond spectroscopy [60].

The Ehrenfest-TDDFT method represents a widely-used hybrid quantum-classical approach, adept at handling nonadiabatic electron-ion dynamics with considerable success in various applications. However, a limitation lies in its representation of nuclei as classical points of charge, causing a lack of decoherence in the method. This absence might lead to the neglect of essential mechanisms contributing to decoherence [61], such as the broadening of the nuclear wave packet and the decrease in the nuclear wave packet overlap. Our study elucidates the effects of classical nuclear motion on changes in nuclear geometry and nuclear Coulomb potentials. The exploration of more intricate nuclear quantum effects surpasses the capabilities of our single trajectory Ehrenfest method, necessitating further research to comprehensively grasp the influence of nuclear motion on CM modes.

ACKNOWLEDGMENTS

W.-D.Y. expresses gratitude to Dr. Bing Sun in University of Chinese Academy of Sciences for engaging in valuable discussions on the density matrix theory and classical field theory. This work is funded by National Natural Science Foundation of China under Grants No. 12104019, No. 12234002, and No. 92250303, and by National Key R&D Program of China under Grants No. 2022YFA1603200 and No. 2022YFA1603201.

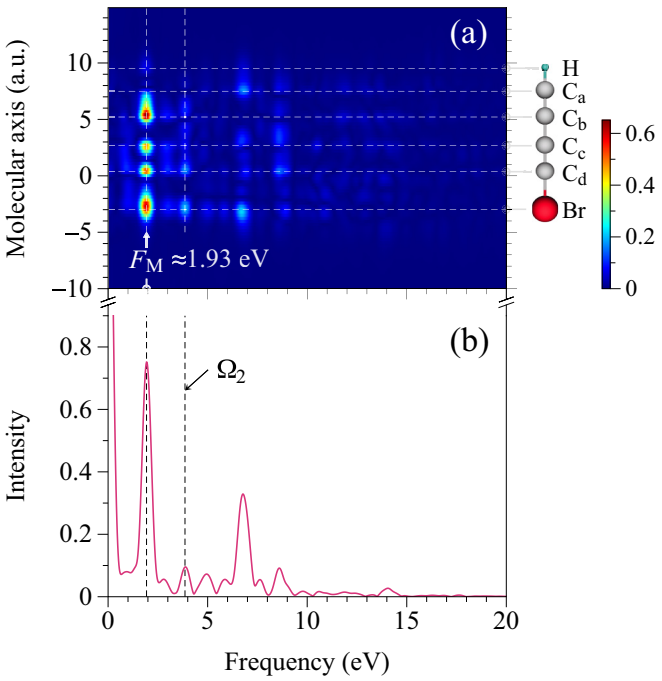

FIG. 6. Frequency analysis of the charge dynamics with the frozen nuclei approximation. (a) Space-frequency analysis for the hole density. F_M: The frequency of CM modes with the maximum intensity. Dashed horizontal lines: Nuclear equilibrium positions of the neutral molecule. Color bar labels the hole density in atomic units. (b) Frequency spectra of the electronic dipole moment. Ω_2: Second harmonic frequency of the F_M.

APPENDIX A: HOLE DENSITY EVOLUTION USING THE FIXED NEUTRAL ELECTRONIC DENSITY

In Fig. 5, we present a comparative analysis of the hole density dynamics, maintaining all parameters identical to those in Fig. 1(a), with the sole exception being the method used to calculate the hole density. In this case, we compute the one-dimensional integrated hole density (Q^h), defined as

$$Q^h(z,t) = \iint Q^H[x,y,z,\mathbf{R}(t),t]dxdy, \qquad \text{(A1)}$$

where Q^H represents the three-dimensional hole density, defined by the difference between the time-independent neutral DFT electronic density with the nuclear geometry at $t = 0$, $\rho^0_{DFT}[\mathbf{r},\mathbf{R}(0)]$, and the time-dependent electronic density from the TDDFT at time t, $\rho^+[\mathbf{r},\mathbf{R}(t),t]$,

$$Q^H[\mathbf{r},\mathbf{R}(t),t] = \rho^0_{DFT}[\mathbf{r},\mathbf{R}(0)] - \rho^+[\mathbf{r},\mathbf{R}(t),t]. \qquad \text{(A2)}$$

As depicted in Fig. 5, during the initial 5 fs, the majority of the hole density is concentrated at the Br site. Between 5 and

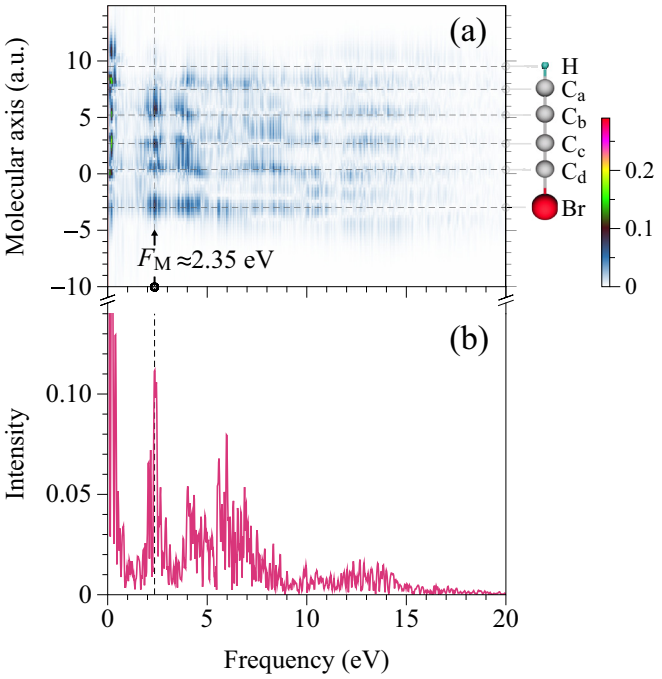

FIG. 7. Frequency analysis of the charge dynamics with an initial 1.2 a_0 stretch of the C_a-C_b bond length. (a) Space-frequency analysis for the hole density. F_M: the frequency of CM modes with the maximum intensity. Dashed horizontal lines: nuclear equilibrium positions of the neutral molecule. Color bar labels the hole density in atomic units. (b) Frequency spectra of the electronic dipole moment.

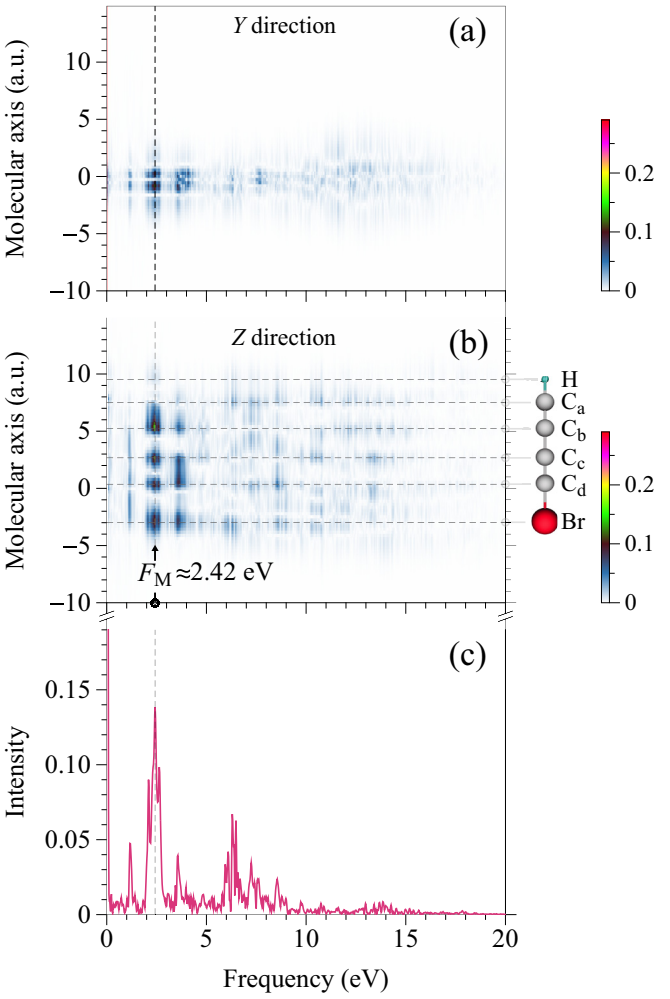

FIG. 8. Frequency analysis of the charge dynamics with an initial 10.21-degree bend in the C_d-Br bond: (a,b) present the space-frequency analysis of the hole density for the frequency components along the *Y* and *Z* axes, respectively, showcasing the frequency of CM modes with the maximum intensity at approximately 2.42 eV. Dashed horizontal lines: Nuclear equilibrium positions of the neutral molecule. Color bar labels the hole density in atomic units. (c) Frequency spectra of the electronic dipole moment.

15 fs, the hole density progressively becomes trapped within the carbon bonds, indicating the emergence of nuclear effects that subsequently impact the hole dynamics. Beyond 15 fs, we observe the hole density dispersing across various regions of the molecule, deviating from the hole patterns presented in Fig. 1(a).

APPENDIX B: CM FREQUENCY ANALYSIS WITH THE FROZEN NUCLEI APPROXIMATION

To illustrate the effects of the nuclear motion on the frequencies of the charge motion, we juxtapose the spatially resolved hole frequency with the frequency spectrum of the electronic dipole moment for comparative purposes. The nuclei are frozen on the neutral equilibrium positions. As illustrated in Fig. 6(a), the space-frequency analysis reveals four distinct spots peaking at $F_M \approx 1.93$ eV, with closely matched intensities that correspond to a prominent peak in the electronic dipole moment's frequency spectra. Upon comparing these frequencies with those in Fig. 2(a), we observe that the frequency distributions in Fig. 6(a) are more pristine and focused around the F_M. Notably, sidebands are absent in this representation, and the second harmonic emerges more clearly. Furthermore, in this case, the nuclei remain fixed at the neutral molecule's equilibrium positions, denoted by the dashed horizontal lines. For each frequency island at 1.93 eV, a preference for concentrating on the nuclear positions is evident.

APPENDIX C: CM FREQUENCY ANALYSIS FOR THE INITIAL STRETCH OF THE TERMINAL C-C BOND

In Figs. 7(a) and 7(b), we present the spatially resolved hole frequencies and the electronic dipole moment's frequency spectra, respectively, following an initial 1.2 a_0 stretch of the terminal C_a–C_b bond length. The space-frequency analysis reveals that the CM modes remain clearly discernible, with evident frequency splitting due to the nuclear motion. The frequency of CM modes with the maximum intensity also aligns with the F_M value of 2.35 eV, corresponding to a distinct peak in the electronic dipole moment's frequency spectra. These results carry two implications. First, despite the terminal C_a–C_b bond exhibiting weaker electronic affinity compared to the halogen site, this bond is still crucial for altering the CM modes and is more effective in causing frequency splitting. Second, the results indicate that the F_M

remains close to the median value of 2.5 eV, as discussed in Fig. 4, suggesting that the CM modes exhibit a certain degree of robustness against the initial C_a-C_b bond length stretch.

APPENDIX D: CM FREQUENCY ANALYSIS FOR THE INITIAL BEND OF THE TERMINAL C-BR BOND

With an initial 10.21-degree bend of the C_d–Br bond, we carry out a space-frequency analysis of the hole density decomposed along the Y and Z axes. Figure 8(a) displays the space-frequency analysis in the Y direction, characterized by the frequency component of the CM modes at 2.42 eV. As shown in Fig. 8(b), in the Z direction, the CM modes are clearly visible, peaking at the same frequency of 2.42 eV. These two components correspond to a pronounced peak in the electronic dipole moment's frequency spectra, as depicted in Fig. 8(c). The F_M is centered at 2.42 eV, which is in close proximity to the median value of 2.5 eV, as shown in Fig. 4.

[1] F. Krausz and M. Ivanov, Rev. Mod. Phys. **81**, 163 (2009).
[2] M. Nisoli, P. Decleva, F. Calegari, A. Palacios, and F. Martín, Chem. Rev. **117**, 10760 (2017).
[3] P. M. Kraus, M. Zürch, S. K. Cushing, D. M. Neumark, and S. R. Leone, Nat. Rev. Chem. **2**, 82 (2018).
[4] P. Peng, C. Marceau, and D. M. Villeneuve, Nat. Rev. Phys. **1**, 144 (2019).
[5] P. M. Kraus, B. Mignolet, D. Baykusheva, A. Rupenyan, L. Horny, E. F. Penka, G. Grassi, O. I. Tolstikhin, J. Schneider, F. Jensen, L. B. Madsen, A. D. Bandrauk, F. Remacle, and H. J. Wörner, Science **350**, 790 (2015).
[6] H. Yong, S. M. Cavaletto, and S. Mukamel, J. Phys. Chem. Lett. **12**, 9800 (2021).
[7] L. He, S. Sun, P. Lan, Y. He, B. Wang, P. Wang, X. Zhu, L. Li, W. Cao, P. Lu, and C. D. Lin, Nat. Commun. **13**, 4595 (2022).
[8] F. Calegari, D. Ayuso, A. Trabattoni, L. Belshaw, S. De Camillis, S. Anumula, F. Frassetto, L. Poletto, A. Palacios, P. Decleva, J. B. Greenwood, F. Martín, and M. Nisoli, Science **346**, 336 (2014).
[9] L. S. Cederbaum and J. Zobeley, Chem. Phys. Lett. **307**, 205 (1999).
[10] A. I. Kuleff, S. Lünnemann, and L. S. Cederbaum, Chem. Phys. **414**, 100 (2013).
[11] E. P. Månsson *et al.*, Commun. Chem. **4**, 73 (2021).
[12] V. Despré and A. I. Kuleff, Phys. Rev. A **106**, L021501 (2022).
[13] J. Breidbach and L. S. Cederbaum, Phys. Rev. Lett. **94**, 033901 (2005).
[14] A. Bruner, S. Hernandez, F. Mauger, P. M. Abanador, D. J. LaMaster, M. B. Gaarde, K. J. Schafer, and K. Lopata, J. Phys. Chem. Lett. **8**, 3991 (2017).
[15] A. D. Dutoi, M. Wormit, and L. S. Cederbaum, J. Chem. Phys. **134**, 024303 (2011).
[16] J. Breidbach and L. Cederbaum, J. Chem. Phys. **118**, 3983 (2003).
[17] P. Ehrenfest, Z. Phys. **45**, 455 (1927).
[18] F. Calvayrac, P.-G. Reinhard, E. Suraud, and C. Ullrich, Phys. Rep. **337**, 493 (2000).
[19] D. Mendive-Tapia, M. Vacher, M. J. Bearpark, and M. A. Robb, J. Chem. Phys. **139**, 044110 (2013).
[20] M. Vacher, M. J. Bearpark, and M. A. Robb, J. Chem. Phys. **140**, 201102 (2014).
[21] M. Vacher, D. Mendive-Tapia, M. J. Bearpark, and M. A. Robb, J. Chem. Phys. **142**, 094105 (2015).
[22] M. Vacher, F. E. Albertani, A. J. Jenkins, I. Polyak, M. J. Bearpark, and M. A. Robb, Faraday Discuss. **194**, 95 (2016).
[23] M. Lara-Astiaso, A. Palacios, P. Decleva, I. Tavernelli, and F. Martín, Chem. Phys. Lett. **683**, 357 (2017).
[24] M. Lara-Astiaso, D. Ayuso, I. Tavernelli, P. Decleva, A. Palacios, and F. Martín, Faraday Discuss. **194**, 41 (2016).
[25] M. Lara-Astiaso, M. Galli, A. Trabattoni, A. Palacios, D. Ayuso, F. Frassetto, L. Poletto, S. De Camillis, J. Greenwood, P. Decleva, J. B. Greenwood, F. Martín, and M. Nisoli, J. Phys. Chem. Lett. **9**, 4570 (2018).
[26] D. Jia, J. Manz, and Y. Yang, J. Phys. Chem. Lett. **10**, 4273 (2019).
[27] N. V. Golubev, T. Begušić, and J. Vaníček, Phys. Rev. Lett. **125**, 083001 (2020).
[28] D. T. Matselyukh, V. Despré, N. V. Golubev, A. I. Kuleff, and H. J. Wörner, Nat. Phys. **18**, 1206 (2022).
[29] A. S. Folorunso, A. Bruner, F. Mauger, K. A. Hamer, S. Hernandez, R. R. Jones, L. F. DiMauro, M. B. Gaarde, K. J. Schafer, and K. Lopata, Phys. Rev. Lett. **126**, 133002 (2021).
[30] K. A. Hamer, F. Mauger, A. S. Folorunso, K. Lopata, R. R. Jones, L. F. DiMauro, K. J. Schafer, and M. B. Gaarde, Phys. Rev. A **106**, 013103 (2022).
[31] F. Mauger, A. S. Folorunso, K. A. Hamer, C. Chandre, M. B. Gaarde, K. Lopata, and K. J. Schafer, Phys. Rev. Res. **4**, 013073 (2022).
[32] W.-D. Yu, H. Liang, L. Geng, and L.-Y. Peng, Phys. Rev. A **107**, 013101 (2023).
[33] A. S. Folorunso, F. Mauger, K. A. Hamer, D. D. Jayasinghe, I. S. Wahyutama, J. R. Ragains, R. R. Jones, L. F. DiMauro, M. B. Gaarde, K. J. Schafer *et al.*, J. Phys. Chem. A **127**, 1894 (2023).
[34] S. Fleischer, Y. Zhou, R. W. Field, and K. A. Nelson, Phys. Rev. Lett. **107**, 163603 (2011).
[35] H. Eshuis and T. Van Voorhis, Phys. Chem. Chem. Phys. **11**, 10293 (2009).
[36] M. Vacher, L. Steinberg, A. J. Jenkins, M. J. Bearpark, and M. A. Robb, Phys. Rev. A **92**, 040502(R) (2015).
[37] K. Saita and D. V. Shalashilin, J. Chem. Phys. **137**, 22A506 (2012).
[38] C. Arnold, O. Vendrell, and R. Santra, Phys. Rev. A **95**, 033425 (2017).
[39] V. Despré, N. V. Golubev, and A. I. Kuleff, Phys. Rev. Lett. **121**, 203002 (2018).
[40] Q. Wu and T. Van Voorhis, Phys. Rev. A **72**, 024502 (2005).
[41] Q. Wu and T. Van Voorhis, J. Chem. Theory Comput. **2**, 765 (2006).
[42] B. Kaduk, T. Kowalczyk, and T. Van Voorhis, Chem. Rev. **112**, 321 (2012).
[43] X. Gonze, B. Seddon, J. A. Elliott, C. Tantardini, and A. V. Shapeev, J. Chem. Theory Comput. **18**, 6099 (2022).
[44] R. S. Mulliken, J. Chem. Phys. **23**, 1833 (1955).

[45] A. E. Clark and E. R. Davidson, Int. J. Quan. Chem. **93**, 384 (2003).
[46] A. D. Becke, J. Chem. Phys. **88**, 2547 (1988).
[47] F. L. Hirshfeld, Theor. Chim. Acta **44**, 129 (1977).
[48] D. D. O'Regan and G. Teobaldi, Phys. Rev. B **94**, 035159 (2016).
[49] D. Kidd, A. S. Umar, and K. Varga, Phys. Rev. B **98**, 075108 (2018).
[50] H. J. Wörner, C. A. Arrell, N. Banerji, A. Cannizzo, M. Chergui, A. K. Das, P. Hamm, U. Keller, P. M. Kraus, E. Liberatore *et al.*, Struct. Dyn. **4**, 061508 (2017).
[51] G. Kolesov, B. A. Kolesov, and E. Kaxiras, Phys. Rev. B **96**, 195165 (2017).
[52] C. Shepard, R. Zhou, D. C. Yost, Y. Yao, and Y. Kanai, J. Chem. Phys. **155**, 100901 (2021).
[53] E. Runge and E. K. U. Gross, Phys. Rev. Lett. **52**, 997 (1984).
[54] N. Tancogne-Dejean *et al.*, J. Chem. Phys. **152**, 124119 (2020).
[55] C. Hartwigsen, S. Goedecker, and J. Hutter, Phys. Rev. B **58**, 3641 (1998).
[56] J. P. Perdew and A. Zunger, Phys. Rev. B **23**, 5048 (1981).
[57] L. Verlet, Phys. Rev. **159**, 98 (1967).
[58] I. Daubechies, J. Lu, and H.-T. Wu, Appl. Comput. Harmon. Anal. **30**, 243 (2011).
[59] A. Deliège and S. Nicolay, Phys. Rev. E **96**, 033307 (2017).
[60] N. V. Golubev, J. Vaníček, and A. I. Kuleff, Phys. Rev. Lett. **127**, 123001 (2021).
[61] M. Vacher, M. J. Bearpark, M. A. Robb, and J. P. Malhado, Phys. Rev. Lett. **118**, 083001 (2017).